Predictive Inverse Model for Advective Heat Transfer in a Planar Fracture with Heterogeneous Permeability

Adam Jacob Hawkins[1,1], Don Bruce Fox[1,1], Donald Koch[2,2], Matthew W Becker[3,3], and Jefferson William Tester[1,1]

[1]Cornell University
[2]Cornell
[3]Department of Geological Sciences, California State University Long Beach

November 30, 2022

Abstract

Identifying fluid flow maldistribution in planar geometries is a well-established problem in subsurface science/engineering. Of particular importance to the thermal performance of Engineered (or "Enhanced") Geothermal Systems (EGS) is identifying the existence of non-uniform (i.e., heterogeneous) permeability and subsequently predicting advective heat transfer. Here, machine learning via a Genetic Algorithm (GA) identifies the spatial distribution of an unknown permeability field in a two-dimensional Hele-Shaw geometry (i.e., parallel-plates). The inverse problem is solved by minimizing the L2-norm between simulated Residence Time Distribution (RTD) and measurements of an inert tracer breakthrough curve (BTC) (C-Dot nanoparticle). Principal Component Analysis (PCA) of spatially-correlated permeability fields enabled reduction of the parameter space by more than a factor of ten and restricted the inverse search to reservoir-scale permeability variations. Thermal experiments and tracer tests conducted at the mesoscale Altona Field Laboratory (AFL) demonstrate that the method accurately predicts the effects of extreme flow channeling on heat transfer in a single bedding-plane rock fracture. However, this is only true when the permeability distributions provide adequate matches to both tracer RTD and frictional pressure loss. Without good agreement to frictional pressure loss, it is still possible to match a simulated RTD to measurements, but subsequent predictions of heat transfer are grossly inaccurate. The results of this study suggest that it is possible to anticipate the thermal effects of flow maldistribution, but only if both simulated RTDs and frictional pressure loss between fluid inlets and outlets are in good agreement with measurements.

Predictive Inverse Model for Advective Heat Transfer in a Planar Fracture with Heterogeneous Permeability

A. J. Hawkins[1,2], D. B. Fox[2], D. L. Koch[2], M. W. Becker[3], and J. W. Tester[2]

[1]Stanford University, Energy Resources Engineering, Stanford, CA 94305.

[2]Cornell University, Robert Fredrick Smith School of Chemical and Biomolecular Engineering, Ithaca, NY 14853.

[3]California State University, Long Beach, Geology Department, Long Beach, CA 90840.

Corresponding author: Adam J. Hawkins (ajh338@cornell.edu)

Key Points:

- Rapid heat transfer accurately predicted at a meso-scale field laboratory.
- Genetic algorithm identified channeled flow via tracer/pressure calibration.
- Principal component analysis reduced the number of solved variables by more than a factor of ten.

Abstract

Identifying fluid flow maldistribution in planar geometries is a well-established problem in subsurface science/engineering. Of particular importance to the thermal performance of geothermal reservoirs is identifying the existence of non-uniform (i.e., heterogeneous) permeability and subsequently predicting advective heat transfer. Here, machine learning via a Genetic Algorithm (GA) identifies the spatial distribution of an unknown permeability field in a two-dimensional Hele-Shaw geometry. The inverse problem is solved by minimizing the L^2-norm between measured and simulated fluid Residence Time Distribution (RTD). Principal Component Analysis (PCA) of spatially-correlated permeability fields enabled reduction of the parameter space by more than a factor of ten and restricted the inverse search to large-scale permeability variations. Thermal experiments and tracer tests conducted at a meso-scale field laboratory in Altona, New York demonstrate that the method accurately predicts the effects of extreme flow channeling on heat transfer in a bedding-plane rock fracture. However, this is only true when the permeability distributions provide adequate matches to both tracer RTD and frictional pressure loss. Without good agreement to frictional pressure loss, it is still possible to match a simulated RTD to measurement, but subsequent predictions of heat transfer are grossly inaccurate. The results of this study suggest that it is possible to anticipate the thermal effects of flow maldistribution, but only if both simulated RTDs and frictional pressure loss between fluid inlets and outlets are in good agreement with measurements.

1 Introduction

Accurate forecasting of heat and mass transfer in two-dimensional planes (e.g., Hele-Shaw cells, groundwater aquifers, microchannels, magma flow etc.) requires adequate specification of reservoir permeability. This is particularly true when non-uniform (i.e., heterogeneous) permeability disrupts the flow pattern between an inlet and outlet. If permeability distributions promote preferential flow paths, such conditions can produce an inlet-outlet "short-circuit" which is directly analogous to electrostatics described by Ohm's law (e.g., Darnton et al., 2001; Levitov and Falkovich, 2016; Oh et al., 2012). This is a well-established problem in subsurface hydrology (e.g., Alley et al., 2002; Black et al., 2017; Cathles, 1990; Doughty, 1999; Guo et al., 2016; Kurowski et al., 1994; Larsson et al., 2013; Moreno and Neretnieks, 1993; Mortada and Nabor, 1961; Subramanian et al., 2013; Tsang and Tsang, 1988; Zouache et al., 2019; etc.). More recently, fluid flow maldistribution has been identified as a key issue that "plagues" (Toma, 2017) energy functional materials and microfluidics (e.g., Al-Housseiny et al., 2012; Babu and Ajayan, 2019; Lagadec et al., 2019; Stone et al., 2004; etc.) and can play a significant role in blood flow maldistribution (e.g., Pries et al., 2010; Qiu et al., 2019; Zouache et al., 2016; etc.)

In subsurface science and engineering, quantitatively characterizing the spatial distribution of permeability is exceptionally challenging. This is particularly true in fractured rock hydrogeology where fracture permeability, k, is proportional to the square of the spacing or "aperture," b, between the upper and lower surfaces ($k = b^2/12$). Therefore, laterally extensive fracture planes can transmit fluids at reservoir-scale (e.g., 100s of meters) through a single fracture while permeabilities can range by orders of magnitude even at the local scale (e.g., centimeters). As a result, it is exceedingly difficult to use local-scale measurements of fracture aperture (e.g., near observation wells) to anticipate reservoir-scale flow patterns.

This difficulty introduces considerable uncertainty into predicting heat and mass transfer in rock fractures and has significant implications for the movement of both subsurface resources (e.g., hot water/steam, petroleum, dissolved minerals, etc.) and contaminants (e.g., radionuclides, fertilizers, chlorinated solvents, etc.). In an Engineered (or "Enhanced") Geothermal System (EGS), for example, commercial success requires development of a deep subsurface heat exchanger capable of heating cold injectate before circulating fluids are produced for direct use or electricity generation. If inlet-outlet short-circuiting reduces the effective heat transfer area, however, then production wells may cool unexpectedly prior to the plant reaching financial maturity (Hawkins et al., 2018). Rapid thermal drawdown at one or more production wells is often referred to as "premature thermal breakthrough" and has challenged the growth of low-grade geothermal resources for decades (e.g., Brown et al., 1999; Hawkins et al., 2018; Horne, 1985; Murphy et al., 1981; Pruess, 1990; Robinson and Tester, 1984, 1986; Robinson et al., 1988; Shook and Suzuki, 2017; Suzuki et al., 2019; Tester et al., 1982, 1989, 2006; etc.).

Here, an inverse model is presented for identifying the spatial distribution of fracture aperture in a two-dimensional plane (i.e., a "Hele-Shaw" geometry) based on calibration to a specified inlet-outlet RTD and frictional pressure loss. The inversion procedure consists of two stages. In the first stage, the inverse problem is solved by minimizing an objective function that compares simulated Residence Time Distribution (RTD) to the measured breakthrough curve (BTC) of an inert tracer. In the second stage, the minimum and maximum fracture aperture is constrained by comparing measured and simulated frictional pressure loss. The resulting fracture aperture field is then used to forecast advective heat transfer using the numerical model summarized in subsection 3.3 and originally presented in Fox et al. (2015).

A Genetic Algorithm (GA), which mimics the optimizing behavior of natural selection, is employed here to solve this highly non-linear inverse problem. Principal Component Analysis (PCA) of self-affine fractures made this problem computationally tractable by reducing the number of optimized variables from thousands to as few as five. As a result of PCA, this global optimizer if forced to investigate the effects of large-scale aperture fluctuations on transport processes that dominate at the reservoir-scale.

The capabilities and predictive value of this novel inversion routine are demonstrated in the results section based on meso-scale experiments performed at a well-characterized field site known as the Altona Field Laboratory (AFL). These field tests targeted a sub-horizontal bedding plane fracture located roughly 7.6 m below ground surface and this target fracture is known to exhibit channeled-flow behavior. An inert tracer test performed under forced-convection between an injector-producer well pair spaced 14.1 m apart provided the measured BTC data. A thermal experiment originally presented in Hawkins et al. (2017a, 2018) provided the temperature measurements needed to evaluate predictions that resulted from the optimized aperture fields and a brief summary of the thermal experiment is provided here in subsection 2.2.

2 Altona Field Laboratory (AFL)

The predictive inverse model described in this study is tested against meso-scale field tests conducted at the Altona Field Laboratory (AFL). This site is located in northeastern New York State near the USA/Canadian border. Since the first five wells were drilled in 2004, the 10 x 10 m five-spot well configuration has been the target of numerous investigations into flow channeling in sparsely-spaced fracture planes (Figure 1). These investigations included geophysical surveys and hydraulic/tracer testing and primarily targeted a sub-horizontal bedding-

plane fracture located roughly 7.6 m below ground surface (Becker and Tsoflias, 2010; Guiltinan and Becker, 2015; Hawkins et al., 2017b; Talley et al., 2005; Tsoflias and Becker, 2008; Tsoflias et al., 2015; etc.). As discussed in Hawkins et al. (2017a, 2018) fluids are highly concentrated in an east-west direction between well 204 and 304. Based on the combined results of numerical models, adsorbing tracer tests, Ground Penetrating Radar (GPR) surveys, and Fiber-Optic Distributed Temperature Sensing (FO-DTS), a narrow channel roughly 1-2 m wide spans the 14.1 m distance between well 204 to the west and well 304 to the east. The first subsection that follows below describes the results of a tracer test performed in 2016 using inert carbon-cored nanoparticles referred to as "C-Dots" (e.g., Hawkins et al., 2017a). Following the description of this tracer test is a brief summary of the heat exchange experiment conducted in 2015 which is described in detail in Hawkins et al. (2017a, 2018).

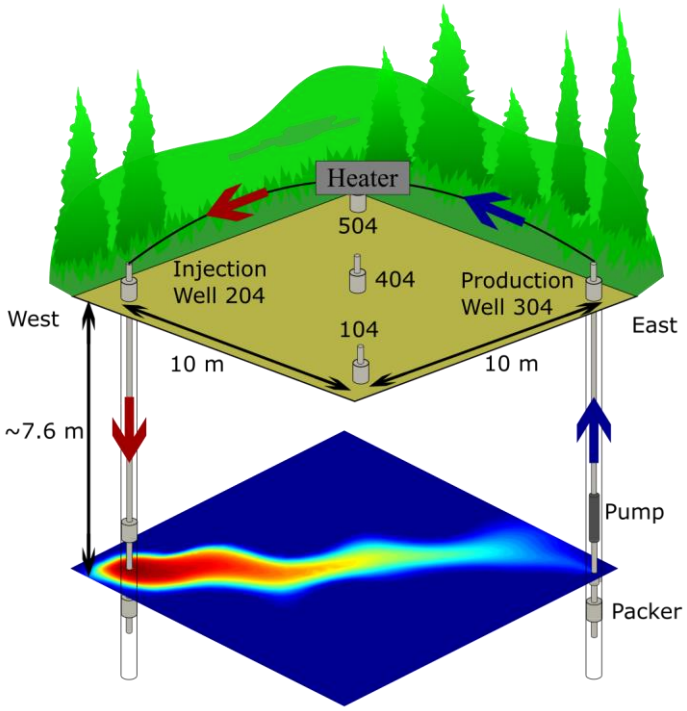

Figure 1. Three-dimensional schematic of the Altona Field Laboratory (AFL) showing the spatial configuration of injection well 204 and production well 304 as well as three monitoring wells (104, 404, and 504). The red and blue arrows depict the circulation pattern introduced during the heat exchange experiment in which hot water continuously circulated through the target fracture for 6 d. The contour map shown at ~7.6 m below ground surface is the temperature distribution predicted after 24 h as a result of the aperture distribution shown in the upper-left corner of Figure 6.

2.1 Inert Tracer Test (2016)

A carbon-cored nanoparticle tracer, or "C-Dots," served as an inert tracer for field testing at the AFL in the summer of 2016. This fluorescent tracer consists of a carbon core decorated with a highly fluorescent polymer (Krysmann et al., 2012). It is ideal for groundwater tracer testing, because it is highly water soluble, inert, environmentally benign, and detectable by

fluorescence at concentrations as low as ~1 ppb in deionized water (Hawkins et al., 2017a; Ray et al., 2009; Subramanian et al., 2013; Zhao, 2015). C-Dots were used in past field tests at the Altona site in the fall of 2015 to estimate the Residence Time Distribution (RTD) between injection well 204 and production well 304 (Hawkins et al., 2017a). A comparison to an organic tracer (phenol) and an anion tracer (iodide) confirmed that the C-Dot nanoparticle tracer behaved conservatively at the Altona site.

A constant volumetric flow rate of 5.82 L/min at the injection/production wells established a steady-state forced-convection hydraulic field (Table 1). A C-Dot mass of 402.2 g was introduced into the formation following the approach described in Hawkins et al. (2017a, 2018) in which a PVC bypass system allowed for introduction of the tracer with minimal disturbance to the subsurface hydraulic gradient field. Polypropylene centrifuge tubes were used to collect 15 mL groundwater samples for laboratory analysis. An ice-filled cooler preserved the fluid samples until the time of analysis by excitation/emission spectra measured by a Cary Eclipse fluorescence spectrophotometer manufactured by Agilent Technologies.

Produced fluids during the tracer test were immediately circulated back into the injection well. A straddle-packer assembly (Lansas Products) hydraulically isolated flow to the target fracture and constrained wellbore storage volume to roughly 3 to 5 L in the injection well and three observation wells. At the production well, a single packer provided hydraulic isolation below the fracture. In the 2015 tracer tests (Hawkins et al., 2017a), the injection well straddle packer assembly reduced wellbore storage to roughly 8 L. In the present study, this volume was reduced further to 5 L.

Table 1. Description of the 2016 inert tracer test and modeled parameters

Symbol	Description	Value	Unit
Q	volumetric flow rate	9.7e-5	m^3/s
μ_w	dynamic viscosity of water	1.0e-3	Pa-s
ρ_w	fluid density	1000	kg/m^3
M_{inj}	[a]tracer mass injected	0.402e-3	kg

[a]tracer injectate (2.895 L) consisted of 4.190 mL of concentrated C-Dot solution (96,000 ppm) added to 2.891 L of groundwater collected from well 304

2.2 Heat Exchange Experiment (2015)

In the fall of 2015, field testing at the AFL provided a low-temperature analog to simulate conditions in an operating geothermal reservoir at meso-scale. For six days, heated injectate (74 °C) circulated through the initially cold (11.7 °C) reservoir (Table 2). A Grundfos submersible pump installed in a shroud assembly maintained a continuous fluid flow rate of 5.7 L/min out of production well 304. All produced fluids were piped through a propane-fired tankless water heater (AO Smith, Model #: T-H3-OS) and reintroduced into well 204. The design and results of the thermal test are described in detail in Hawkins et al. (2017a, 2017b, 2018).

During reservoir heating, a Fiber-Optic Distributed Temperature Sensor (FO-DTS) (Sensornet Ltd, Model: Oryx) recorded the spatial distribution of fracture/matrix heat exchange in ten monitoring boreholes located throughout the 10 x 10 m well field. The FO-DTS measured temperature along a 1400 m cable wrapped around ten externally threaded schedule-80 Polyvinyl Chloride (PVC) pipes. Wrapping the fiber-optic cables resulted in roughly 70 to 140 temperature measurements along the 1.5 to 3 m long pipes.

FO-DTS temperature measurements were recorded in the dry, bulk rock matrix above the target fracture with roughly 0.5 m of undisturbed rock remaining between the deepest measurement and the target fracture. Fracture fluid temperatures could then be determined based on an error function extrapolation of the measured temperature data to the depth of the target fracture (Hawkins et al., 2017a). In addition to the FO-DTS temperature measurements, temperature sensors measured fluid temperature in three monitoring wells (Solinst Leveloggers, Model #: 3001) and in the production well (RBR, Model: Solo T).

Table 2. Description of the 2015 thermal test and modeled parameters

Symbol	Description	Value	Unit
Q	[a]volumetric flow rate	9.5e-5	m^3/s
T_r	[b]ambient rock temperature	11.7	°C
T_w	[b]injected water temperature	74.0	°C
$C_{p,w}$	specific heat of water	4200	J/kg-K
$C_{p,r}$	[c]specific heat of sandstone	1000	J/kg-K
μ_w	dynamic viscosity of water	1.0e-3	Pa-s
λ_r	[b]thermal conductivity of Potsdam Sandstone	7.6	W/m-K
ρ_r	[b]density of Potsdam Sandstone	2500	kg/m^3
ρ_w	fluid density	1000	kg/m^3
t_{th}	total elapsed time of the thermal test	5.184e5	s

[a]volumetric flow rate into injection well 204 and out of production well 304 were equal and constant
[b]source: Hawkins et al. (2017a)
[c]source: Robertson (1988)

3 Inverse Problem Description and Numerical Methods

An inverse problem is a computational formulation where one attempts to calculate the parameters that describe a system, making use of a set of data or observations. It is the reverse of a forward model which calculates the response of a system for a given set of parameter values. Mathematically, the inverse problem is formulated as $d_i = F(x_j)$, where d_i is the vector of data or observations and F is a model often comprised of algebraic and/or differential equation or sets of equations which depend on x_j. The inverse problem is solved by determining the x_j given d_i based on minimizing an "objective function" which evaluates the fitness of a calculated value to measurement.

For the inverse problem presented here, x_j represents local values of the fracture aperture field, F is a numerical model describing the behavior of the injected C-Dot tracer (subsection 2.1), and d_i is the measured BTC of tracer introduced at a single injection well and eluted from a single production well under steady-state hydraulic conditions. The description of the permeability field is first discussed (subsection 3.1), followed by an explanation of how tracer RTD is calculated (subsection 3.2). Finally, the numerical model of heat transfer described in Fox et al. (2015) is summarized in subsection 3.3.

3.1 Spatially-correlated Fracture Aperture Distribution

Laminar fluid flow through naturally permeable materials such as rock fractures commonly exhibit variable flow paths as a result of spatially fluctuating permeability. The permeability field adopted here is a self-affine description where relatively large-scale variations in permeability (small frequencies, long wavelengths) are more important for describing heat and

mass transport compared to small-scale variations (Feder, 1988; Falconer, 2003). The primary purpose of the self-affine model is to systematically generate target permeability distributions with different flow path geometries which, in effect, "trains" the optimization routine. Core samples containing rock fractures from wide-ranging geographies have revealed fracture apertures to have a self-affine spatial correlation which suggests that their subsequent permeability distributions are also self-affine (Brown et al., 1986; Glover et al., 1998; Plouraboué et al., 1995; Ponson et al., 2007; Schmittbuhl et al., 1993, 1995, 2008). Below is a detailed description of the varying permeability field with a self-affine spatial correlation.

The permeability field described here is based on the equivalency to fracture aperture described as $k = b^2/12$, where k and b are fracture's permeability and aperture, respectively. The spatially varying aperture field can therefore be described as $b(x, y) = \langle b \rangle + h(x, y)$, where $\langle b \rangle$ is the mean aperture value and h is the local aperture fluctuation. A Hurst roughness coefficient, ζ, and a spatial correlation function are used to describe the spatially-correlated aperture field (e.g., Di Federico and Neuman, 1997, 1998) and the variogram function, γ, required for describing the spatial correlation is

$$\gamma(d) \equiv \langle [h(\mathbf{p}) - h(\mathbf{p} + d)]^2 \rangle = 2[\langle h^2 \rangle - \langle h(\mathbf{p}) h(\mathbf{p} + d) \rangle], \quad (1)$$

where $\mathbf{p}$ is a position vector on the surface of the 2-D fracture and d is the displacement distance from $\mathbf{p}$. To have a self-affine geometry, Equation 1 must have a scaling behavior that follows $\gamma(d) = a|d|^{2\zeta}$, where a is an arbitrary constant.

Based on core samples, Hurst coefficients range from 0.5 for sandstone (e.g., Boffa et al., 1999; Ponson et al., 2007) to 0.8 for granite (e.g., Schmittbuhl et al., 1993, 1995; Plouraboué et al., 1995) and a surface with a lower Hurst coefficient is rougher. An algorithm modified from Méheust and Schmittbuhl (2001) generated numerous hypothetical self-affine fracture aperture distributions. Random seeding using Fast Fourier Transforms (FFTs) produces hypothetical fracture aperture fields that are both statistically isotropic and self-affine (Figure 3).

3.2 Numerical Model for Calculation of Residence Time Distribution (RTD)

Laminar flow of an incompressible fluid between two parallel plates is described by the Hele-Shaw equation, which is often referred to as the "cubic law" in fractured rock hydrogeology (Witherspoon et al.,1980). As described in Fox et al. (2015), the velocity field can be derived by the finite element method treatment of

$$-\nabla \cdot \left(\frac{b^3}{12\mu} \nabla P \right) = 0, \quad (2)$$

where P is the hydraulic fluid pressure and μ is the fluid's dynamic viscosity, assuming the lubrication approximation is valid for the specified length scales. The velocity averaged across the fracture aperture is then given by $\langle \mathbf{v} \rangle = -b^2/(12\mu)\, \nabla P$. With velocity specified, the transport of tracer particles in the permeability field follows the governing equation

$$b \frac{\partial c}{\partial t} + b \langle \mathbf{v} \rangle \cdot \nabla c = 0, \quad (3)$$

where c is tracer concentration and t is time.

The modeling approach described by Equation 3 neglects longitudinal/transverse dispersion resulting from the combined effects of velocity and concentration gradients across the fracture aperture (i.e., Taylor-Aris dispersion). Instead, tracer RTD variance is produced solely

by non-uniform velocity in the plane of the fracture. These velocity variations result from the combined effects of dipole-flow and heterogeneous permeability. As discussed in Hawkins et al. (2017a, 2018), this approach is more appropriate for tracer transport between parallel plates where Taylor-Aris dispersion, as described by Horne and Rodriguez (1983), should be negligible relative to velocity variations resulting from dipole flow and heterogeneous permeability (Detwiler et al., 2000; Neretnieks, 1980; Novakowski et al., 1985; Robinson et al., 1988; Tang et al., 1981).

Flow through the fracture plane is induced by steady-state circulation between an injection and production well and there is a no flux condition on the boundaries of the fracture. The wells are modeled as an internal boundary with 64 FEM computational nodes rather than a single node to avoid singularities in velocity. The total flux across the internal boundaries representing the wells is equal to the volumetric flow rate, Q.

To model a pulse injection tracer test, the initial condition is $c(x, y, 0) = 0$, and the boundary condition at the location of the injection well $\mathbf{p}_{inj}$ is $c(\mathbf{p}_{inj}, t) = m_p \delta(t - t_0)/Q$, where m_p is the mass of injected tracer, δ is the Dirac delta function, and t_0 is the time of instantaneous tracer injection. Additionally, there is a no mass flux condition along the lateral boundary of the fracture. The concentration of tracer at the production well with time produces a tracer breakthrough curve that is a result of the aperture field and resulting flow in the fracture. By simulating an instantaneous injection of an inert tracer, the concentration curve represents the RTD of the permeable reservoir.

3.3 Numerical Model for Advective Heat Transfer

After the permeability field from the inverse search has been obtained, it is used to calculate advective heat transfer and subsequently forecast production well fluid temperature as a function of time. The comparison of predicted temperatures resulting from the optimized aperture field with measured temperatures recorded at the AFL determines how effective the inversion scheme was in predicting a reservoir's thermal performance. The temperature field is determined using the numerical model presented in Fox et al. (2015). It calculates the heat transport within the fracture aperture field using the FEM and couples it to a boundary integral description of the heat conduction in the impermeable material surrounding the fracture plane. Note that this simulation neglects buoyancy effects and assumes the fluid and rock properties are negligible.

4 Inversion Algorithm

To solve for the permeability field, an inversion algorithm was developed using reduced order modeling and a global optimizer. The optimization algorithm is used to minimize the error against a simulated tracer RTD curve, expressed as an objective function. The L^2-norm error is used as the objective function and is defined as $L_d^2 = \left\|\hat{d}_i - d_i\right\|^2 / \|d_i\|$, where d_i is the vector of measured concentration data as a function of time while the $\hat{d}_i$ terms are the simulated values resulting from a candidate aperture field of the inverse search.

A GA is used for the parameter optimization and a reduced order model of the aperture field is obtained using PCA, an algorithm that determines the dominant modes of a system. The description and application of PCA for the problem is first presented, followed by the explanation of how the GA is used to solve the inverse problem.

4.1 Principal Component Analysis

Principal Component Analysis (PCA) (sometimes called "proper orthogonal decomposition") is a statistical tool common to engineering sciences. PCA is particularly useful in the analysis of datasets with a large number of independent variables (e.g., Cui et al., 2015; Johnston et al. 2009, Li and Jarfarpour, 2010; van Doren et al., 2006; etc.). In the current study, PCA reduces the number of unknown parameters requiring estimation via the inverse model by targeting larger, spatially-correlated regions of the aperture field. Rather than independently estimating each fracture aperture value in the FEM mesh, PCA restricts the inverse search to reservoir-scale heterogeneities by varying the intensity of PCA modes (eigenvectors) with the largest modal coefficients (eigenvalues).

The first step in PCA is to calculate the covariance matrix between independent variables in a dataset. Then, the eigenvectors and eigenvalues of the covariance matrix are calculated. Each eigenvector represents a "mode" of the dataset (Figure 2). The eigenvalues represent the relative strength of each mode. For spatially-correlated fractures, the mode with the largest eigenvalue corresponds to spatial variations over relatively large areas of the fracture.

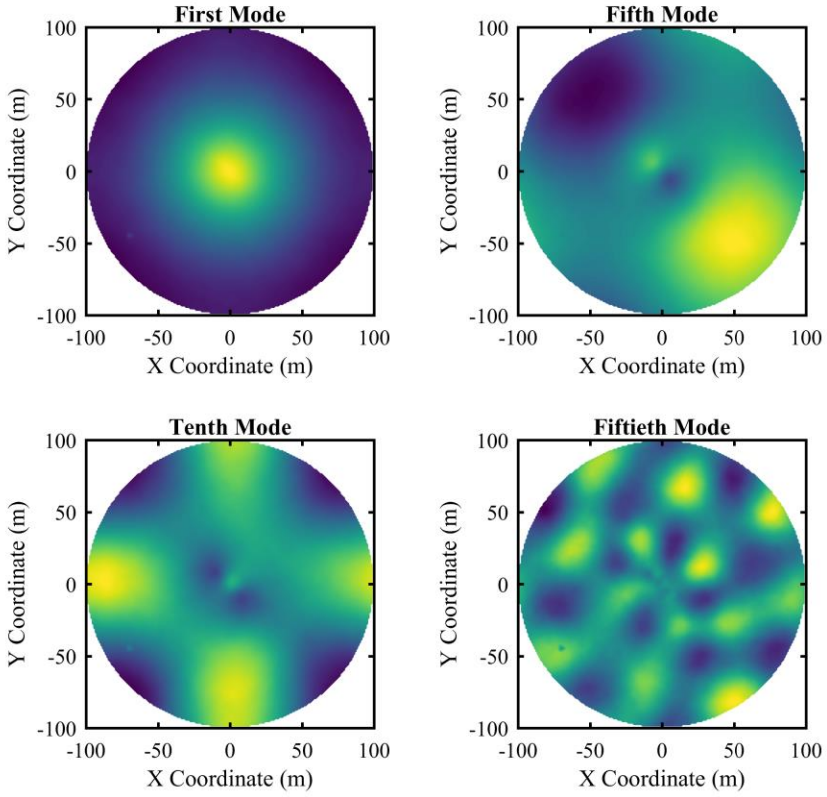

Figure 2. Modes resulting from PCA of a hypothetical circular fracture with a radius of 100 m. The color scale is arbitrary as the strength of each mode fluctuates during the Genetic Algorithm (GA) optimization. The first mode (largest-scale variations) is shown in the upper-left corner and is compared to modes that describe spatial variations at smaller scale including the fifth mode (upper right), the tenth mode (bottom left), and the fiftieth mode (bottom right).

For PCA of a generic data set, X_{ij}, describing realization j and variable i where n variables each have a mean of zero across m realizations, the covariance matrix, $C_{ii'}$, between two variables is given by

$$C_{ii'} = \sum_{j=1}^{m} X_{ij} X_{i'j}. \quad (4)$$

For a discrete heterogeneous fracture represented by nodes on a computational mesh, n is the number of nodes and m is the number of aperture fields generated. Once the eigenvectors (or "modes") and eigenvalues (or "coefficients") of the covariance matrix have been determined, an aperture field in the matrix of observations can be reproduced by knowing the modes of the entire dataset and the coefficients for the specific aperture field, such that

$$w_i = \sum_{j=1}^{p} \mathbf{\Phi}_{ij} \beta_j + \langle w \rangle, \quad (5)$$

where w_i is the fracture aperture at node i, $\mathbf{\Phi}_{ij}$ is the matrix of PCA modes, β_j are the coefficients of the PCA modes, and $\langle w \rangle$ is the mean fracture aperture. The reproduced aperture field is identical to the original if p is equal to n, the total number of nodes. If p is less than n, then Equation 5 produces a simplified aperture field that neglects small-scale spatial variations as

illustrated in Figure 3. In addition, entirely new aperture distributions result from altering the magnitude of the mode coefficients. Any new distribution will have a unique aperture field, but the eigenvectors of its covariance matrix (i.e. its PCA modes) are identical to the original data set. A description of the FEM mesh and parameters of the PCA are provided in Table 3.

Table 3. Description of the finite element mesh and the principal component analysis

Symbol	Description	Value
n_{nodes}	number of finite element nodes	7196
n_{elem}	number of finite elements	7100
n_{inj}	number of injection well nodes	64
n_{prod}	number of production well nodes	64
n_{PCA}	number of samples for PCA	5000
ζ	[a]Hurst roughness coefficient	0.5

[a]average value for sandstone based on Boffa et al. (1999) and Ponson et al. (2007)

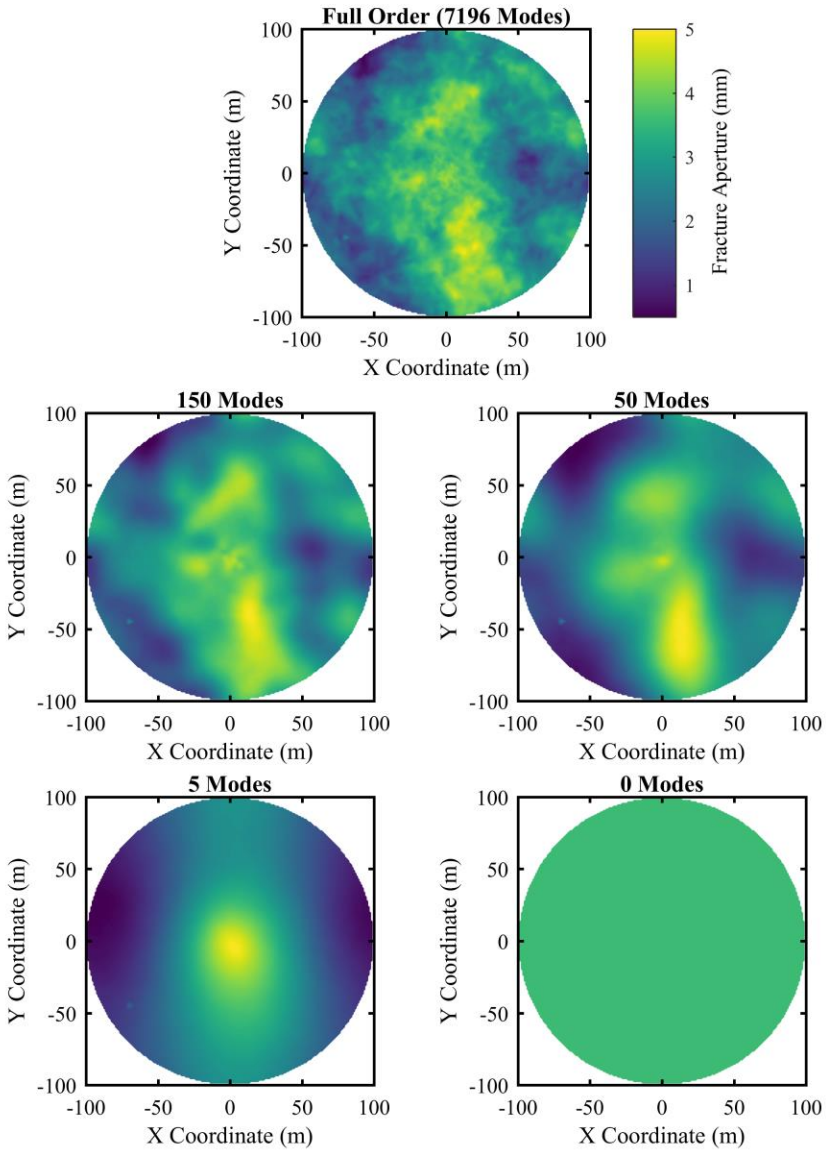

Figure 3. Hypothetical 2-D fracture aperture field (top) compared to reduced order aperture fields ranging from 150 modes (middle left) to 0 modes (i.e., homogeneous) (bottom right).

4.2 Genetic Algorithm

The challenge in solving an inverse problem for heterogeneous permeability is that the number of unknown variables is typically too large for conventional inversion routines (McLaughlin and Townley, 1996). For a circular fracture with non-uniform aperture, accurate numerical simulations of heat and mass transport could easily require thousands of specified aperture values in the two-dimensional field. Therefore, an attempt to solve an inverse problem by independently varying the values at each node in the computational mesh is inefficient considering the computational time required and the relatively small influence of local-scale aperture fluctuations on tracer and thermal transport at the reservoir scale. As discussed in the previous subsection, PCA simplified this problem by allowing the inverse model to vary the

aperture field in a spatially-correlated fashion. As a result, the only information that must be specified, *a-priori*, is the Hurst roughness coefficient, the number of PCA modes required in solving the inverse problem, and (if desired) the mean or the minimum and maximum aperture.

Even after PCA, there remains several challenging aspects in successfully employing an inverse model for heterogeneous aperture fields, including: (1) the inverse problem is non-linear; (2) there remains a relatively large number of unknown variables; and (3) there are likely many local minimums of the objective function. For these reasons, a stochastic inverse search method is preferable to a deterministic minimization which would require long computation times to search the parameter space and suffers from inefficiencies while searching near local minima. One commonly used metaheuristic optimization method is a Genetic Algorithm (GA). It is designed to mimic natural selection and minimize an objective function, $f(x_j)$, where x_j is a set of parameter values (e.g., Cao et al., 2012; Hornby et al., 2011; Tasan and Gen, 2012). The GA is similar to natural selection in that the "fitness" of an initial population is quantified and new "generations" are produced by "breeding" and/or "mutating" individuals in the population that are specified using a suitable selection function. Once the desired conditions for termination are met (e.g., number of generations, target objective function, computation time, etc.), the optimization is complete (Figure 4).

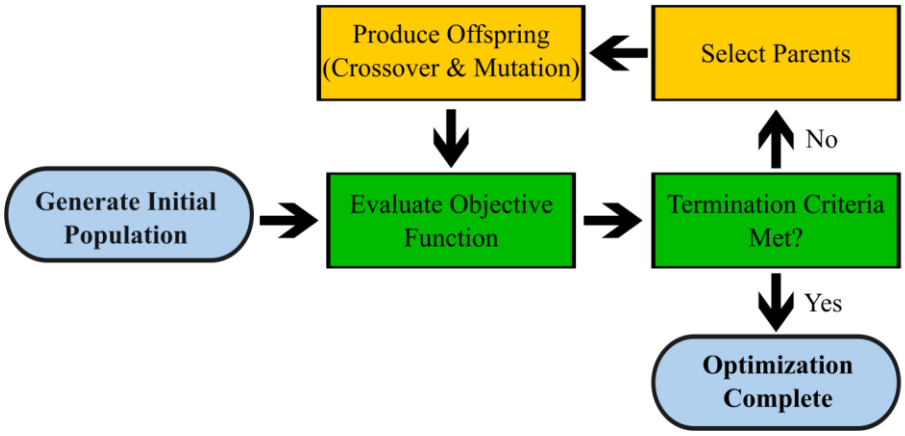

Figure 4. Flow diagram for the Genetic Algorithm (GA) demonstrating the optimization process.

For the first stage of the optimization, the parameter values for the GA are the PCA mode coefficients, β, and the min/max fracture aperture. In stage 2, the min and max fracture apertures are specified based on agreement between measured and simulated frictional pressure loss. For both stages, the objective function is the L^2-norm between measured and simulated tracer BTCs. Parameters of the initial population were determined using the range of β values given an arbitrary standard deviation used during PCA. The parent selection function selects individuals for "reproduction" and this study adopted the tournament style. A genetic crossover function generated 80% of the "offspring" and a mutation function produced the remaining 20%. The mutation function randomly changes the "genes" of individual parents, which in this study are the PCA mode coefficients or the min/max aperture and a maximum of 60 generations is specified as the termination criteria (Table 4).

Table 4. Input parameters of the two-stage GA optimization

Symbol	Description	Stage 1	Stage 2
n_{pop}	population size in each generation	144	120
n_{gens}	maximum number of generations	60	60
n_{elite}	elite fit carryover	2	2
n_{var}	number of solved variables	[a]1-152	150
w_{min}	minimum aperture	[b]n/a	0.02e-3 m
w_{max}	maximum aperture	[b]n/a	8e-3 m
f_{cross}	crossover fraction	0.8	0.8

[a]ranges from 1 (i.e., 0 modes/homogeneous) to 152 (i.e., 150 modes and minimum/maximum aperture)
[b]stage 1 heterogeneous scenarios consider both the minimum and maximum aperture as unknown variables solved by the GA

5 Results

The results of the optimization routine are broken down into two subsections. The first subsection describes the results of the two-stage optimization. The second subsection compares predicted temperatures with measurements at the AFL.

5.1 Optimized Aperture Field

As discussed in subsection 4.2, the main input parameter required for the first stage of this optimization is the number of PCA modes selected for optimization. With the number of modes selected and the initial range of mode coefficients and apertures specified, the GA searches for an optimal aperture distribution by varying modal coefficients and the upper/lower aperture boundaries. Four scenarios are considered in the first stage ranging from a homogeneous aperture field (i.e., zero PCA modes) to a heterogeneous aperture field composed of 150 PCA modes.

The first scenario of the first stage is presented as a base case in which the fracture aperture field is homogeneous. As shown in the top row of Figure 5, a uniform aperture of 0.51 mm results in reasonably good agreement with tracer measurements (Table 5). Both the simulated and measured modal residence times (i.e., elapsed time corresponding to peak tracer concentration) occur at 20 min. The model-fit peak concentration (0.0361 min^{-1}) at the modal residence time is in slight disagreement with measurement (0.04 min^{-1}) and the L^2-norm for the base case is 0.22.

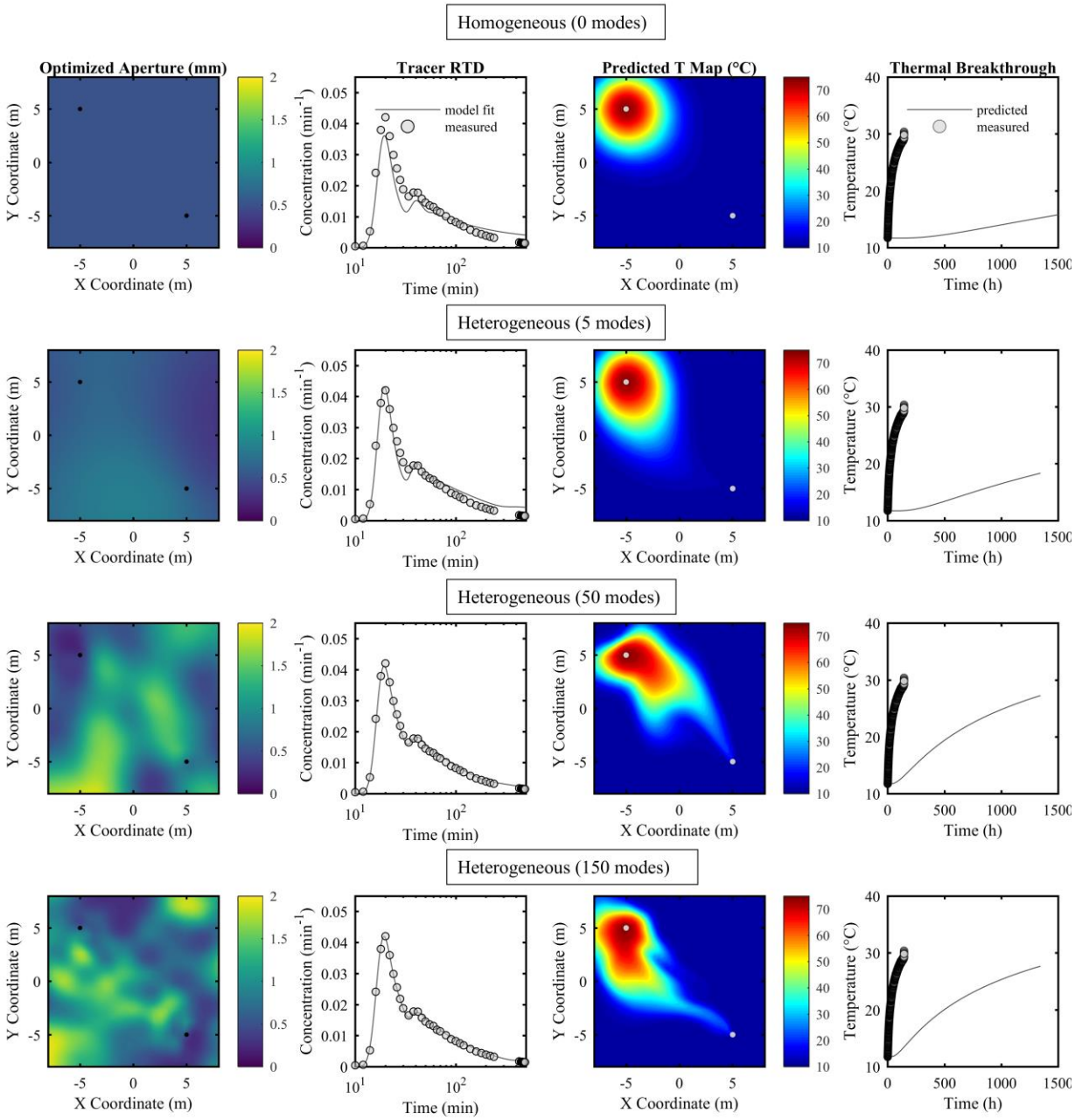

Figure 5. Preliminary results of the four scenarios prior to considering frictional pressure loss (i.e. stage 1-1 to 1-4). Optimized aperture distributions are shown in the first column and their resulting match to the measured inert tracer BTC are shown in the second column. Subsequent predictions of advective heat transfer are shown in the third and fourth columns. The contour plot in the third column shows the temperature distribution in the plane of the target fracture predicted after 6 d of continuous hot water circulation and the fourth column compares predicted and measured production well temperatures. The four scenarios include the base case homogeneous aperture field (first row) and three heterogeneous cases in which the number of modes solved by the GA varies from 5 (second row) to 150 (fourth row). Note that the bimodal distributions of tracer breakthrough (second column) results from reinjection of produced fluids

from well 304 back into well 204. Tracer concentration is normalized by dividing the product of concentration and volumetric flow rate by tracer mass injected. Measured production well temperatures first published in Hawkins et al. (2017a).

Table 5. Final results of the two-stage optimization, preliminary results of the four scenarios considered in the first stage, and predicted production well temperature, T_{prod}, after 6 d of hot water circulation

Stage	Number of Modes Optimized	Mean Aperture (min, max) [mm]	L^2-norm	[a]ΔP [Pa]	[b]T_{prod} (t = 6 d) [°C]
2	150	2.5 [c](n/a, n/a)	0.11	-548	26.0
1-1	0 (homogeneous)	0.51 (n/a, n/a)	0.22	-11,191	11.70
1-2	5	0.61 (0.31, 0.87)	0.15	-6317	11.73
1-3	50	0.83 (0.16, 2.0)	0.06	-11,274	13.0
1-4	150	0.84 (0.24, 2.2)	0.04	-5636	13.3

[a]measured frictional pressure loss is -433 Pa (Table 6)
[b]measured temperature at the end of the 6 d heat exchange experiment is 29.3 °C (Hawkins et al., 2017a) (Figure 5)
[c]maximum and minimum aperture specified at fixed values of 0.02 and 8 mm, respectively

The second scenario considers a total of seven unknown variables which include the minimum/maximum fracture aperture and the coefficients of the first five PCA modes. The GA used a population of 144 and allowed up to 60 generations before terminating the optimization routine. The optimization identified a minimum and maximum aperture of 0.31 and 0.87 mm, respectively, which resulted in an L^2-norm of 0.15 and a noticeably improved match to the peak tracer concentration (second row in Figure 5).

Two additional scenarios considered a larger number of PCA modes (50 and 150). With 50 PCA modes optimized, the GA identified a minimum and maximum aperture of 0.16 and 2.0 mm, respectively, and resulted in an L^2-norm of 0.06. With 150 modes optimized, the minimum and maximum aperture identified are 0.24 and 2.2 mm, respectively, and resulted in an L^2-norm of 0.04. For the scenarios in which the number of PCA modes were 5, 50, and 150, the resulting mean of the optimized aperture field were 0.61, 0.83, and 0.84 mm, respectively.

Increasing the number of PCA modes identified by the GA from 0 to 5 resulted in a nearly perfect match to the modal residence time and the peak tracer concentration and a minor mismatch of the trough measured at ~30 min. With 50 modes, there is a nearly perfect overall match between the model fit and measured breakthrough curves. With 150 modes, the roughness of the permeability field is noticeably increased but the match to the inert tracer curve is relatively unchanged compared to the 50 mode scenario.

Even though the third and fourth scenarios result in a nearly perfect match to the BTC measured at the AFL, these aperture distributions do not guarantee accurate predictions of advective heat transfer (Hawkins et al., 2017a). This is true because an inert tracer BTC provides an estimation of interwell fluid volume whereas the extent of advective heat transfer is dominated by the effective heat transfer surface area (Hawkins et al., 2018). As discussed in Hawkins (2020), however, advective heat transfer can be anticipated if a model aperture field provides good agreement with both frictional pressure loss and reservoir transit time.

The first four scenarios discussed above specified a fixed volumetric flow rate into the injection well and out of the production well. The FEM solver subsequently calculated the pressure field and velocity field. During the inversion routine, the objective function evaluated

the tracer fit, but gave no consideration to the agreement between measured and simulated pressures in the injector or producer. Based on the pressure drop simulated by the permeability fields shown in column 1 of Figure 5, however, there is considerable disagreement between the simulated and measured frictional pressure loss between the injection and production well. Simulated pressure loss between the injection well and production well for 0, 5, 50, and 150 modes are -11,911, -6317, -11,274, and -5636 Pa, respectively. In contrast, the pressure measured in production well 304 is 433 Pa less than the pressure measured at injection well 204 (Table 6).

Table 6. Hydraulic head measurements from 2012 and parameter values used to calculate frictional pressure loss

Symbol	Description	Value	Unit
Q	volumetric flow rate	7.00e-5	m^3/s
Δh_{204}	[a]injection well hydraulic head change at Q	-6.35e-3	m
Δh_{304}	[a]production well hydraulic head change at Q	-50.51e-3	m
g	gravitational acceleration	9.8	m/s^2
ρ_w	fluid density	1000	kg/m^3
ΔP	[b]calculated frictional pressure loss	-433	Pa

[a]hydraulic head measured via Solinst Leveloggers, Model #: 3001 and reported value is the average across 16 or more measurements recorded over a time interval of at least 30 min.
[b]frictional pressure loss, ΔP, calculated as $\Delta P = \rho_w g(\Delta h_{304} - \Delta h_{204})$

Based on Equation 2, the relatively small pressure drop measured at the Altona site suggests the true fracture aperture is larger than the aperture field identified in any of the four scenarios considered during stage one of the optimization. Therefore, the second stage of the optimization searched for a larger mean aperture by fixing the minimum and maximum apertures at values of 0.02 and 8.0 mm, respectively. These boundaries were determined based on manually varying the min/max apertures of the fourth scenario until the resulting aperture fields provided good agreement to measured pressure loss.

With the inverse search forced towards larger apertures, stage 2 of the optimization identified an aperture field with a mean of 2.5 mm and produced good agreement between measured and simulated tracer RTD (L^2-norm is 0.11). The resulting RTD is presented in Figure 6 and shows relatively good agreement to measurement. The resulting pressure difference is -548 Pa and is in relatively good agreement with the measured value of -433 Pa compared to the results of the first stage where simulated pressure losses ranged from -11,911 to -5636 Pa.

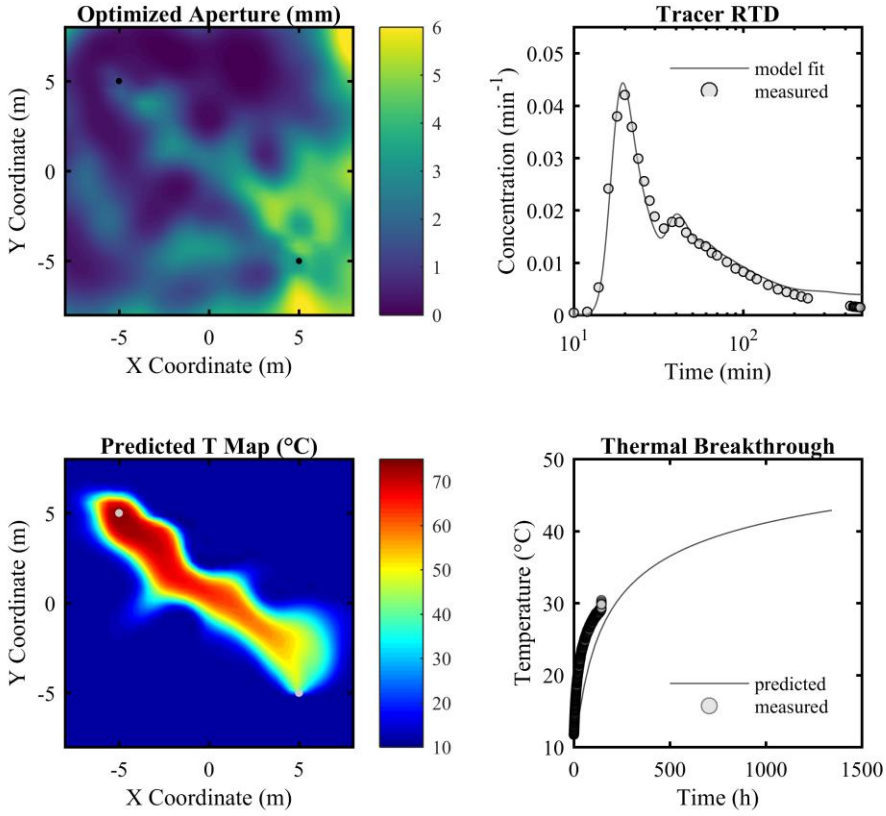

Figure 6. Optimized aperture field (top left) and the resulting simulation compared to measured tracer breakthrough (top right) while considering both RTD and frictional pressure loss. The bottom row shows the subsequent forward-model prediction of advective heat transport. Predicted temperature simulated after 6 d of hot water injection is shown on the bottom left and a comparison between measured and predicted thermal breakthrough is shown on the bottom right.

5.2 Temperature Predictions

Production well temperature predictions were made as described in subsection 3.3 for the optimized aperture field (Figure 6) as well as the four preliminary aperture fields identified during the first stage of the two-stage optimization (Figure 5). In this subsection, the results of the final optimized aperture field will be discussed first followed by a comparison to predictions resulting from the first stage of the optimization. A comparison between these simulations and measured production well temperature rise at the AFL provide an evaluation of the inversion routine's predictive capabilities.

With good agreement to both residence time distribution and frictional pressure loss, the optimized aperture field predicted that production well fluid temperatures would rise 4 ℃ in 35 h. By the end of the 6 d heat exchange experiment, predicted production well temperature reaches 26.0 ℃. For comparison, measured production well temperature rises 4 ℃ in 7.3 h and reaches 29.3 ℃ after 6 d.

Even though the L^2-norm of the final optimization is larger than the best results from the stage 1 preliminary optimization (Table 5), the temperature predictions from stage 2 are

479 substantially more accurate than any of the four scenarios of stage 1. For all four scenarios of the
480 first stage the predicted thermal breakthrough times were substantially delayed relative to the
481 final result of the two-stage optimization. Despite the ideal match to RTDs shown in column 2 of
482 Figure 5, predicted production well temperatures for all four first-stage scenarios disagree with
483 the measured temperature recorded over the 6 d thermal test described in subsection 2.2. For the
484 homogeneous base case, predicted production well temperature rises 4 ℃ in ~61 d whereas
485 measured production fluids rise an equivalent temperature in just 7.3 h. The three subsequent
486 scenarios that solve for varying PCA modes (5, 50, and 150) reduces this disagreement, but
487 predictions are still off by at least a factor of 30. For the 5 and 50 mode scenarios, the predicted
488 time before production well fluids increase 4 ℃ is ~37 and ~11 d, respectively. For the 150
489 mode scenario, this predicted time is ~10 d.

490 **6 Conclusion**

491 We present a novel inverse model that identifies the spatial distribution of heterogeneous
492 fracture aperture/permeability based on calibration to measured inert tracer breakthrough curves
493 (BTCs). The approach used Principal Component Analysis (PCA) to force the inverse search to
494 investigate large-scale spatial fluctuations in fracture aperture. As a result, a Genetic Algorithm
495 (GA) efficiently solved the inverse problem and identifies a simplified aperture field that
496 provides good agreement to the Residence Time Distribution (RTD) and frictional pressure loss.

497 Meso-scale experiments conducted at the Altona Field Laboratory (AFL) demonstrated
498 that the method can identify an aperture field by minimizing the L^2-norm of simulated RTDs
499 compared to the breakthrough curve measured via the C-Dot nanoparticle tracer. With this
500 aperture field specified, a predictive forward model of advective heat transfer accurately
501 forecasted rapid thermal breakthrough between the same injector/producer well pair. This
502 channeled-flow behavior resulted from a narrow preferential flow path (~1-2 m) that caused an
503 inlet/outlet "short circuit." This result is in very good agreement with independent measurements
504 via Ground Penetrating Radar (GPR), a network of thermal sensors, and the results of an
505 adsorbing tracer test (Hawkins et al., 2017a, 2018).

506 Accurate predictions of heat transfer are only possible, however, if the aperture field
507 produces good agreement to both transit time and frictional pressure loss. In fact, even a uniform
508 (i.e., homogeneous) aperture field can provide reasonable agreement to the measured BTC while
509 providing a poor prediction of thermal transport. With a homogeneous aperture field, production
510 well temperature rises 4 ℃ in ~63 d whereas measured temperature rises 4 ℃ in just 7.3 h. In
511 contrast, the aperture field that provides good agreement to both frictional pressure loss and
512 residence time distribution predicts a 17.6 ℃ temperature rise in 8 d compared to a measured
513 temperature rise of 17.6 ℃ in 6 d. This result is consistent with the observation that a tracer RTD
514 alone cannot independently establish both volume and effective surface area of a one-
515 dimensional reservoir (Hawkins et al., 2018).

516 The results of this study have significant implications for tracer and hydraulic testing in
517 fractured rock reservoirs. Of particular importance is the observation that the RTD of an inert
518 tracer in a fracture is independent of the mean and range of fracture aperture magnitude. This
519 reinforces the conclusions of Hawkins et al. (2017a, 2018) which suggest that inert tracer testing
520 should not be considered as a means by which fracture aperture magnitude is estimated. Instead,
521 inert tracer testing provides an approximation of interwell fluid volume. Meanwhile, measured
522 frictional pressure loss does provide an approximation of mean fracture aperture. The predictive

model shown in Figure 6 provides reasonably accurate estimates of the thermal response because the identified aperture field produces an interwell fluid volume in good agreement with tracer tests and a mean aperture that is in good agreement with measured frictional pressure loss.

Acknowledgements

Support for A.J.H provided by the TomKat Center for Sustainable Energy at Stanford University. This material is based upon work supported by the U.S. Department of Energy, Office of Energy Efficiency and Renewable Energy (EERE), Office of Technology Development, Geothermal Technologies Program, under Award Numbers DE EE0002767, DE EE0006764 and DE EE0006763. Additional financial assistance was provided by the National Science Foundation's Earth Energy IGERT program and the Cornell Energy Institute. The authors thank the State University of New York, Plattsburgh and the William H. Miner Agricultural Research Institute for field assistance and for providing access to their facilities, including their Environmental Laboratory and the Altona Flat Rock site. The authors would also like to thank numerous individuals who aided field testing, including Ivan Beentjes, Sean Hillson, Koenraad Beckers, and Maciej Lukawski. All data supporting analysis and conclusions are publically available through the U.S. Department of Energy's Geothermal Data Repository at https://gdr.openei.org.

References

Al-Housseiny, T., Tsai, P. A., & Stone, H. A. (2012), Control of interfacial instabilities using flow geometry. *Nature Physics*, 9, 757-750.

Alley, W. M., Healy, R. W., LaBaugh, J. W., & Reilly, T. E. (2002), Flow and storage in groundwater systems. *Science*, 296, 1985-1990.

Babu, G., & Ajayan, P. M. (2019), Good riddance, dendrites. *Nature Energy*, 4, 631-632.

Becker, M. W., & Tsoflias, G. P. (2010), Comparing flux-averaged and resident concentration in a fractured bedrock using ground penetrating radar. *Water Resources Research*, 46, W09518, doi:10.1029/2009WR008260.

Black, J. H., Woodman, N. D., & Barker, John A. (2017), Groundwater flow into underground openings in fractured crystalline rocks: an interpretation based on long channels. *Hydrogeology Journal*, 25, 445-463.

Boffa, J. M., Allain, C., Chertcoff, R., Hulin, J., Plouraboué, F., & Roux, S. (1999), Roughness of sandstone fracture surfaces: Profilometry and shadow length investigations. *European Physical Journal B*, 7, 179-182.

Brown, S. R., Kranz, R., & Bonner, B. (1986), Correlation between the Surfaces of Natural Rock Joints. *Geophysical Research Letters*, 13, 1430-1433.

Brown, D., DuTeaux, R., Kruger, P., Swenson, D., & Yamaguchi, T. (1999), Fluid circulation and heat extraction from engineered geothermal reservoirs. *Geothermics*, 28, 553-572.

Cao, K., Huang, B., Wang, S., & Lin, H. (2012), Sustainable land use optimization using boundary-based fast genetic algorithm. *Computers, Environment and Urban Systems*, 36, 257-269.

Cathles, L. M. (1990), Scales and effects of fluid flow in the upper crust. *Science*, 248, 323-329.

Cui, T., Marzouk, Y. M., & Willcox, K. E. (2015), Data-driven model reduction for the Bayesian solution of inverse problems. *International Journal for Numerical Methods in Engineering*, 102, 966-990.

566 Darnton, N., et al. (2001), Hydrodynamics in 2 ½ dimensions: making jets in a plane. *Journal of*
567 *Physics: Condensed Matter*, 13, 4891-4902.
568 Detwiler, R. L., Rajaram, H., & Glass, R. J. (2000), Solute transport in variable-aperture
569 fractures: An investigation of the relative importance of Taylor dispersion and
570 macrodispersion. *Water Resources Research*, 36, 1611-1625.
571 Di Federico, V., & Neuman, S. P. (1997), Scaling of random fields by means of truncated power
572 variograms and associated spectra. *Water Resources Research*, 33, 1075-1085.
573 Di Federico, V., & Neuman, S. P. (1998), Flow in multiscale log conductivity fields with
574 truncated power variograms. *Water Resources Research*, 34, 975-987.
575 Doughty, C. (1999), Investigation of conceptual and numerical approaches for evaluating
576 moisture, gas, chemical, and heat transport in fractured unsaturated rock. *Journal of*
577 *Contaminant Hydrology*, 38, 69-106.
578 Falconer, K. (2003), *Fractal Geometry: Mathematical Foundations and Application*. John Wiley
579 & Sons, Chichester, England, 2nd edition.
580 Feder, J. (1988), *Fractals* (*Physics of Solids and Liquids*). Plenum Press, New York, NY.
581 Fox, D. B., Koch, D. L., & Tester, J. W. (2015), The effect of spatial aperture variations on the
582 thermal performance of discretely fractured geothermal reservoirs. *Geothermal Energy*,
583 3, 1-29.
584 Glover, P. W. J., Matsuki, K., Hikima, R., & Hayashi, K. (1998), Fluid flow in synthetic rough
585 fractures and application to the Hachimantai Geothermal Hot Dry Rock Test Site.
586 *Journal of Geophysical Research*, 103, 9621-9635.
587 Guiltinan, E., & Becker, M. W. (2015), Measuring well hydraulic connectivity in fractured
588 bedrock using periodic slug tests. *Journal of Hydrology*, 521, 100-107.
589 Guo, B., Fu, P., Hao, Y., Peters, C. A., & Carrigan, C. R. (2016), Thermal drawdown-induced
590 flow channeling in a single fracture in EGS. *Geothermics*, 61, 46-62.
591 Hawkins, A. J., Fox, D. B., Becker, M. W., & Tester, J. W. (2017a), Measurement and
592 simulation of heat exchange in fractured bedrock using inert and thermally degrading
593 tracers. *Water Resources Research*, 53, doi: 10.1002/2016WR019617.
594 Hawkins, A. J., Becker, M. W., & Tsoflias, G. P. (2017b), Evaluation of inert tracers in a
595 bedrock fracture using ground penetrating radar and thermal sensors. *Geothermics*, 67,
596 86-94.
597 Hawkins, A. J., Becker, M. W., & Tester, J. W. (2018), Inert and adsorptive tracer tests for field
598 measurement of flow-wetted surface area. *Water Resources Research*, 54, 5341-5358.
599 Hawkins, A. J. (2020), Unknown interfacial surface area at low Reynolds number. Under peer-
600 review for publication in *Physical Review Fluids*.
601 Hornby, G. S., Lohn, J. D., & Linden, D. S. (2011), Computer-automated evolution of an X-band
602 antenna for NASA's Space Technology 5 Mission. *Evolutionary Computation*, 19, 1-23.
603 Horne, R. N., & Rodriguez, F. (1983), Dispersion in tracer flow in fractured geothermal systems.
604 *Geophysical Research Letters*, 10, 289-292.
605 Horne, R. N. (1985), Reservoir engineering aspects of reinjection. *Geothermics*, 14, 449-457.
606 Johnston, P. B., Atkinson, T., Barker, J., & Odling, N. (2009), Constraining the uncertainty in
607 fracture geometry using tracer tests. *Hydrogeology Journal*, 17, 527-539.
608 Krysmann, M. J., Kelarakis, A., Dallas, P., & Giannelis. E. P. (2012), Formation mechanism of
609 carbogenic nanoparticles with dual photoluminescence emission. *Journal of the American*
610 *Chemical Society*, 134, 747-750.

Kurowski, P., Ippolito, I., Hulin, J. P., Koplik, J., & Hinch, E. J. (1994), Anomalous dispersion in a dipole flow geometry. *Physics of Fluids*, 6, 108-117.

Lagadec, M. F., Zahn, R., & Wood, V. (2019), Characterization and performance evaluation of lithium-ion battery separators. *Nature Energy*, 4, 16-25.

Larsson, M., Doughty, C., Tsang, C. F., & Niemi, A. (2013), Understanding the effect of single-fracture heterogeneity from single-well injection-withdrawal (SWIW) tests. *Hydrogeology Journal*, 21, 1691-1700.

Levitov, L., & Falkovich, G. (2016), Electron viscosity, current vortices and negative nonlocal resistance in graphene. *Nature Physics*, 12, 672-676.

Li, L., & Jafarpour, B. (2010), Effective solution of nonlinear subsurface flow inverse problems in sparse bases. *Inverse Problems*, 26(10), 105016.

McLaughlin, D., & Townley, L. R. (1996), A reassessment of the groundwater inverse problem. *Water Resources Research*, 32, 1131-1161.

Méheust, Y., & Schmittbuhl, J. (2001), Geometrical heterogeneities and permeability anisotropy of rough fractures. *Journal of Geophysical Research: Solid Earth*, 106, 2089-2102.

Mohajeri Khameneh, P., Mirzaie, I., Pourmahmoud, N., Rahimi, M., & Majidyfar, S. (2010), A numerical study of single-phase forced convective heat transfer in tube in tube heat exchangers. *International Journal of Mechanical, Aerospace, Industrial, Mechatronic and Manufacturing Engineering*, 4, 958-963.

Moreno, L., & Neretnieks, I. (1993), Flow and nuclide transport in fractured media: The importance of the flow-wetted surface for radionuclide migration. *Journal of Contaminant Hydrology*, 13, 49-71.

Mortada, M., & Nabor, G. W. (1961), An approximate method for determining areal sweep efficiency and flow capacity in formations with anisotropic permeability. *Society of Petroleum Engineers Journal*, 16, 277-286.

Murphy, H. D., Tester, J. W., Grigsby, C. O., & Potter, R. M. (1981), Energy extraction from fractured geothermal reservoirs in low-permeability crystalline rock. *Journal of Geophysical Research*, 86, 7145-7158.

Neretnieks, I. (1980), Diffusion in the rock matrix: An important factor in radionuclide retardation?, *Journal of Geophysical Research*, 85, 4379-4397.

Novakowski, K. S., Evans, G. V., Lever, D. A., & Raven, K. G. (1985), A field example of measuring hydrodynamic dispersion in a single fracture. *Water Resources Research*, 21, 1165-1174.

Oh, K. W., Lee, K., Ahn, B., & Furlani, E. P. (2012), Design of pressure-driven microfluidic networks using electric circuit analogy. *Lab on a Chip*, 12, 515-545.

Plouraboué, F., Kurowski, P., Hulin, J. P., Roux, S., & Schmittbuhl, J. (1995), Aperture of rough cracks. *Physical Review E*, 51, 1675-1685.

Ponson, L., Auradou, H., Pessel, M., Lazarus, V., & Hulin, J. P. (2007), Failure mechanisms and surface roughness statistics of fractured Fontainebleau sandstone. *Physical Review E*, 76, 1-7.

Pries, A. R., Höpfner, M., le Noble, F., Dewhirst, M. W., & Secomb, T. W. (2010), The shunt problem: control of functional shunting in normal and tumour vasculature. *Nature Reviews Cancer*, 10, 587-593.

Pruess, K. (1990), Modeling of geothermal reservoirs: Fundamental processes, computer simulation and field applications. *Geothermics*, 19, 3-15.

656 Qiu, Y., Myers, D. R., & Lam, W. A. (2019), The biophysics and mechanics of blood from a
657 materials perspective. *Nature Reviews Materials*, 4, 294-311.
658 Ray, S. C., Saha, A., Jana, N. R., & Sarkar, R. (2009), Fluorescent carbon nanoparticles:
659 Synthesis, characterization, and bioimaging application. *Journal of Physical Chemistry*
660 *C*, 113, 18546-18551.
661 Robinson, B. A., & Tester, J. W. (1984), Dispersed fluid flow in fractured reservoirs: An
662 analysis of tracer-determined residence time distributions. *Journal of Geophysical*
663 *Research*, 89, 10374-10384.
664 Robinson, B. A., & Tester, J. W. (1986), Characterization of flow maldistribution using inlet-
665 outlet tracer techniques: An application of internal residence time distributions. *Chemical*
666 *Engineering Science*, 41, 469-483.
667 Robinson, B. A., Tester, J. W., & Brown, L. F. (1988), Reservoir sizing using inert and
668 chemically reacting tracers. *SPE Formation Evaluation*, 2, 227-234.
669 Schmittbuhl, J., Gentier, S., & Roux, S. (1993), Field measurements of the roughness of fault
670 surfaces. *Geophysical Research Letters*, 20, 639-641.
671 Schmittbuhl, J., Schmitt, F., & Scholz, C. (1995), Scaling invariance of crack surfaces. *Journal*
672 *of Geophysical Research: Earth Surface*, 100, 5953-5973.
673 Schmittbuhl, J., Steyer, A., Jouniaux, L., & Toussaint, R. (2008), Fracture morphology and
674 viscous transport. *International Journal of Rock Mechanics and Mining Sciences*, 45,
675 422-430.
676 Shook, G. M., & Suzuki, A. (2017), Use of tracers and temperature to estimate fracture surface
677 area for EGS reservoirs. *Geothermics*, 67, 40-47.
678 Stone, H. A., Stroock, A. D., & Ajdari, A. (2004), Engineering flows in small devices:
679 Microfluidics toward a lab-on-a-chip. *Annual Review of Fluid Mechanics*, 36, 381-411.
680 Subramanian, S. K., Li, Y., & Cathles, L. M. (2013), Assessing preferential flow by
681 simultaneously injecting nanoparticle and chemical tracers. *Water Resources Research*,
682 49, 29-42.
683 Suzuki, A., Ikhwanda, F., Yamaguchi, A., & Hashida, T. (2019), Estimations of fracture surface
684 area using tracer and temperature data in geothermal fields. *Geosciences*, 9, 425-446.
685 Talley, J., Baker, G. S., Becker, M. W., & Beyrle, N. (2005), Four dimensional mapping of tracer
686 channelization in subhorizontal bedrock fractures using surface ground penetrating radar.
687 *Geophysical Research Letters*, 32, doi:10.1029/2004GL021974.
688 Tang, D. H., Frind, E. O., & Sudicky, E. A. (1981), Contaminant transport in fractured porous
689 media: Analytical solution for a single fracture. *Water Resources Research*, 17, 555-564.
690 Tasan, A. S., & Gen, M. (2012), A genetic algorithm based approach to vehicle routing problem
691 with simultaneous pick-up and deliveries. *Computers & Industrial Engineering*, 62, 137-
692 158.
693 Tester, J. W., Bivins, R. L., & Potter, R. M. (1982), Interwell tracer analyses of a hydraulically
694 fractured geothermal reservoir. *SPE Journal*, 22, 537-554.
695 Tester, J. W., Murphy, H. D., Grigsby, C. O., Potter, R. M., & Robinson, B. A. (1989), Fractured
696 geothermal reservoir growth induced by heat extraction. *SPE Reservoir Engineering*, 4,
697 97-104.
698 Tester et al. (2006), The future of geothermal energy. Prepared by the Massachusetts Institute of
699 Technology, under Idaho National Laboratory subcontract no. 63 00019 for the U.S.
700 Department of Energy, Assistant Secretary for Energy Efficiency and Renewable Energy,
701 Office of Technologies, p 358. ISBN-10:0486477711, ISBN-13:978-0486477718.

Toma, F. M. (2017), Disentangling interfacial energies. *Nature Energy*, 3, 6-7.
Tsang, Y. W., & Tsang, C. F. (1988), Flow and tracer transport in fractured media: A variable aperture channel model and its properties. *Water Resources Research*, 24, 2049-2060.
Tsoflias, G. P., & Becker, M. W. (2008), Ground-penetrating radar response to fracture-fluid salinity: Why lower frequencies are favorable for resolving salinity changes. *Geophysics*, 73, J25-J30.
Tsoflias, G. P., Perll, C., Baker, M., & Becker, M. W. (2015), Cross-polarized GPR imaging of fracture flow channeling. *Journal of Earth Science*, 26, 776-784.
van Doren, J. F. M., Markovinović, R., & Jansen, J. D. (2006), Reduced-order optimal control of water flooding using proper orthogonal decomposition. *Computational Geosciences*, 10, 137-158.
Witherspoon, P. A., Wang, J. S. Y., Iwai, K., & Gale, J. E. (1980), Validity of cubic law for fluid flow in a deformable rock fracture. *Water Resources Research*, 16, 1016-1024.
Zhao, Y. (2015), The use of nanoparticles to assess subsurface flow heterogeneity, *Ph.D Dissertation*, Cornell University.
Zouache, M. A., Eames, I., Klettner, C. A., & Luthert, P. J. (2016), Form, shape and function: segmented blood flow in the choriocapillaris. *Scientific Reports*, 6, 1-13.
Zouache, M. A., Eames, I., Klettner, C. A., & Luthert, P. J. (2019), Flow and passive transport in planar multipolar flows. *Journal of Fluid Mechanics*, 858, 184-227.